

State-by-state emission spectra fitting for non-equilibrium plasmas: OH spectra of surface barrier discharge at argon/water interface

Jan Voráč, Petr Synek, Vojtěch Procházka, Tomáš Hoder

Department of Physical Electronics, Masaryk University, Kotlářská 2, 61137 Brno, Czech Republic

E-mail: vorac@mail.muni.cz

Abstract. Optical emission spectroscopy applied to non-equilibrium plasmas in molecular gases can give important information on basic plasma parameters, including the rotational, vibrational temperatures and densities of the investigated radiative states. In order to precisely understand the non-equilibrium of rotational-vibrational state distribution from investigated spectra without limiting presumptions, a state-by-state temperature-independent fitting procedure is the ideal approach. In this paper we present a novel software tool developed for this purpose, freely available for scientific community. The introduced tool offers a convenient way to construct Boltzmann plots even from partially overlapping spectra, in user-friendly environment.

We apply the novel software to the challenging case of OH spectra in surface streamer discharges generated from the triple-line of argon/water/dielectrics interface. After the barrier discharge is characterised by ICCD and electrical measurements, the spatially and phase resolved rotational temperatures from $N_2(C-B)$ and $OH(A-X)$ spectra are measured, analysed and compared. The precise analysis shows that $OH(A)$ states with quantum numbers ($v' = 0, 9 \leq N' \leq 13$) are overpopulated with respect to the found two-Boltzmann distribution. We hypothesise that fast vibrational-energy transfer is responsible for this phenomenon observed here for the first time. Finally, the vibrational temperature of the plasma and the relative populations of hot and cold $OH(A)$ states are quantified spatially and phase resolved.

PACS numbers: 52.30.-q, 52.50.Dg, 52.70.-m

Keywords: optical emission spectroscopy, batch processing, *massive OES*, spectra fitting, atmospheric pressure, surface barrier discharge, triple-line, water, hydroxyl, OH

Submitted to: *J. Phys. D: Appl. Phys.*

1. Introduction

Optical emission spectroscopy is a powerful non-invasive tool to investigate non-equilibrium plasmas [1, 2, 3, 4, 5]. Nowadays, crucial parameters such as electric field [6, 7, 8], electron density [9, 10, 11] or densities of important species [12] can be determined by methods of optical emission spectroscopy with high resolution and practically for any plasma of interest. In the case of the molecular spectra, also the rotational temperature as a measure for gas temperature can be obtained. Specair programme [13] offers a commercial solution and is nowadays widely used for this purpose. Other programmes like LIFBASE [14] or PGOPHER [15] are available for free and their functionality partially overlaps with Specair. Nevertheless, due to the transient nature of plasmas and various (de)excitation mechanisms participating in different timescales on population of different rotational states, the determination of the rotational temperature, or densities of these states, is not simple. A typical example is the spectroscopy of the OH radical in water containing discharges [16]. A more detailed approach is needed to investigate these spectra in non-equilibrium plasmas as recently reviewed in [17].

In this article, we present a new tool for state-by-state temperature-independent spectra fitting for molecular spectra of non-equilibrium plasmas. We combine this approach with our previously published tool *massiveOES* [18, 19] for processing of large spectroscopic data (semi-automated methods become very handy if large amount of spatially or temporally highly resolved spectra has to be processed). We apply these tools to investigate the spatially and phase resolved OH spectra in surface barrier discharge emerging at the triple-line (triple-junction) [20] of argon/water/fused silica interface. Plasmas generated at the triple-line at atmospheric pressure feature usually high temperature and electric field gradients as a result of the presence of strong charge separation in the narrow sheath [21, 22]. This feature can be important in treatment of sensitive or bio-medical samples [23], or when trying to understand the detailed plasma-initiated chemistry in surface treatment of polymers [24].

In general, the interest to study water-containing plasmas increased in last years enormously [25]. This fact is in direct connection to plasma applications in wastewater treatment [26, 27] and especially in plasma-medicine [28]. Due to the fact that these applications are operated in atmospheric pressure gases, the nature of these plasmas is highly transient and detailed and spatiotemporally resolved spectra analysis is required to understand their non-equilibrium. We hope that for this purpose the tool introduced in this article will be welcome by scientific community dealing with molecular spectroscopy for plasmas in various applications, not only at atmospheric pressure.

2. Experimental setup and data acquisition

The electrode arrangement is based on the standard surface barrier discharge configuration, see figure 1. Two metal electrodes (copper foil) are glued to opposite

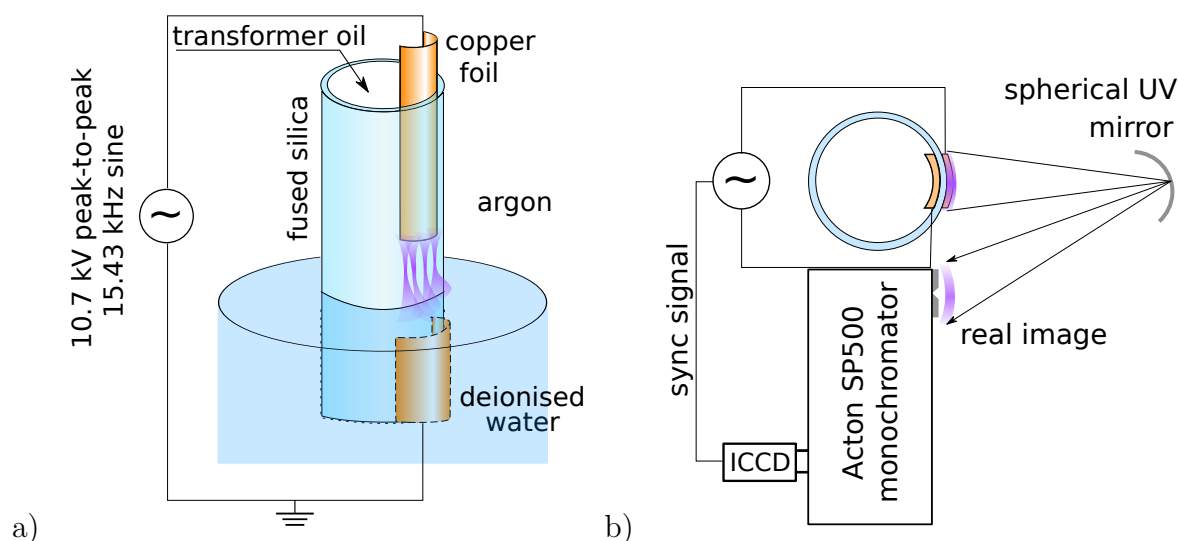


Figure 1. Experimental setup: (a) Schematic sketch of the discharge reactor (detailed description of electrical circuit is omitted for brevity), (b) the scheme of optical detection setup.

sides of a dielectric sheet (fused silica). The dielectric sheet is curved and forms a jacket of a cylindrical cuvette such that one electrode is glued on the outside and the other is on the inside. The cuvette is filled with transformer oil, so the discharges are forced to appear on the outside. The cuvette with the electrodes is placed in a sealed chamber rinsed with argon (1.4 slm flow). The purity of the environment was checked indirectly by observing nitrogen bands in the discharge emission. Based on the fact that nitrogen bands intensity was at least two orders of magnitude smaller than the bands of OH radical or argon lines, the residual nitrogen content is considered negligible. In this particular experiment we add 1 sccm of nitrogen gas to argon on purpose to get second molecular spectra to compare results of OH measurement with[‡].

The chamber is partially flooded with deionised water such that the outer electrode is submerged. In this way, the water forms an additional dielectric barrier and the discharges are thus not in direct contact with the electrode.

Whole circuit consists of reactor chamber and parallel ballast capacitance to minimize resonance shifts due to surface charging (and consequently prevent fluctuation of applied voltage amplitude). The outer submerged electrode is earthed, whereas the inner is driven by sinusoidal alternating voltage with 5.4 kV amplitude at resonant frequency of 15 kHz. Electrical measurements were performed with voltage probe (Tektronix P6015A) and self assembled BNC current probe both connected to a high-resolution and high-sampling rate oscilloscope (Keysight DSO-S 204A). Imaging of the discharge was performed with an ICCD camera (PI-MAX3 1024RB-25-FG-43) equipped with standard objective lens.

[‡] Results for OH measurements show no difference for discharge with and without the 1 sccm of nitrogen gas flow.

For spectroscopic measurements, a real image of the discharge is formed at an input slit of a monochromator (Acton SP-500) using a spherical mirror (25.4 mm diameter, 100 mm focal length, UV enhanced aluminium surface, Thorlabs). The angle between the light direction and the optical axis of the mirror is kept as small as possible to minimise the astigmatic deformation of the image. By using a mirror we can avoid chromatic error. This is critical particularly for argon discharges with water vapour, as the emission is found particularly in the near UV and near IR, spectrally separated by hundreds of nanometres, causing serious shifts in the optical power of lenses. The light enters the monochromator through a $20\ \mu\text{m}$ slit, is dispersed by a grating (3600 grooves/mm, HUV blaze) and collected by an ICCD camera (PI-MAX3 1024RB-25-FG-43). A thin line parallel to the electric field vector in the centre of the electrodes was observed with radial width of the slit opening. This gives a radial selection of obtained spectra. The whole discharge length of ca. 9 mm was imaged to 780 pixels, giving theoretical spatial resolution of 11 micrometers along the discharge axis. Due to weak signal, however, spatial integration was necessary as part of the data processing, reducing the spatial resolution to few tenths of a millimetre, see section 3 for details.

The camera exposure was synchronised with the discharge driving voltage. The positive and negative half-cycles were acquired separately. To obtain sufficient signal-to-noise ratio, the signal was accumulated over 10^6 discharge periods on the CCD chip before readout. The (0,0), (1,1) and (2,2) bands of OH ($A\ ^2\Sigma^+ \rightarrow X\ ^2\Pi$) transition in the spectral region from 306 nm to 318 nm were observed. Because the grating dispersed too well, it was not possible to capture the spectral region of interest at once. Instead, three adjacent spectral windows were acquired, in the respective ranges (305.84–310.86) nm, (308.91–313.89) nm and (312.82–317.75) nm. The last spectral window was acquired with 3×10^6 accumulations to enhance the signal-to-noise ratio of the weaker spectral lines with higher J' and v' quantum numbers.

Another spectral window in the range (333.67–338.61) nm was recorded for reference. This window contains the (0,0) band of the N_2 ($C\ ^3\Pi_u \rightarrow B\ ^3\Pi_g$) transition. The rotational temperature obtained from this band is believed to reliably reflect the translational temperature of gas [19, 29, 30, 31].

In further text, the electronic states will be labelled only by the first letter for brevity, e.g. state $\text{N}_2(\text{C})$ or transition $\text{N}_2(\text{C-B})$.

3. Data processing

The dark current was subtracted from the acquired images. The relative spectral sensitivity was determined using a calibrated deuterium lamp and the images were corrected accordingly. Examples are shown in figure 2. The shown examples are vertically cropped to the region of interest and vertically binned with a bin size of 7 pixels to emphasise an unwanted deformation of the image in the monochromator. The input slit is imaged as a curved line, the wavelength calibration must therefore be performed for each vertical position accordingly. In this work, we assume, that

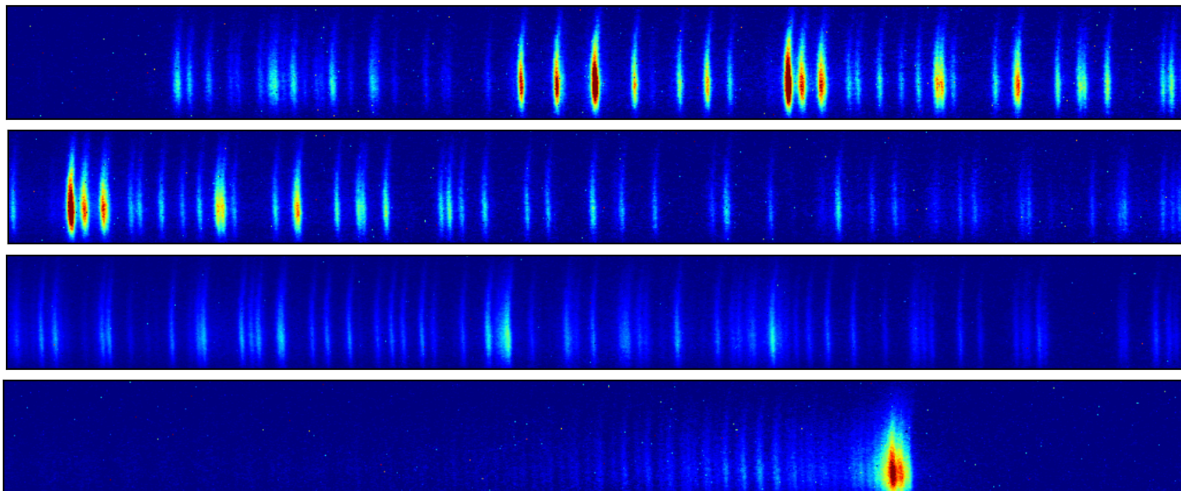


Figure 2. An example of spectroscopic image of the discharge in the positive half-cycle of the applied voltage after dark current subtraction and spectral sensitivity correction. Spectral ranges (305.84–310.86) nm, (308.91–313.89) nm, (312.82–317.75) nm and (333.67–338.61) are shown, respectively. The shown images are vertically cropped to the region of interest and partially vertically binned with a bin size of 7 pixels. The vertical distance corresponds to axial position. The triple-line interface is at the bottom and the discharges propagate upwards.

the deformation results in constant shift of the spectrum along the wavelength-axis and the wavelength resolution is constant. The wavelength calibration is performed by comparing the measured spectrum to a simulation, as described below.

The rotational temperature of $N_2(C)$ is obtained by comparing the measurement with a simulation[§], minimising the sum of squared residuals. Details are described in [19]. First, the wavelengths of the measurement and of the simulation must be matched. For this step, a synthetic spectrum with roughly correct temperature is prepared. Corresponding positions in the simulation and the measurement are identified by visual comparison. This is tricky particularly for the (0,0) band of $N_2(C-B)$ transition, as only one band head is available at 337.2 nm and the maximum of the R-branch around 336.7 nm shifts with rotational temperature. Other ($v', v'' = v'$) bands of $N_2(C-B)$ are too weak due to significantly smaller Franck-Condon factors [32] and are thus unobservable even at high vibrational temperatures [19]. In more energetic discharges with hydrogen content, also emission of $NH(A^3\Pi \rightarrow X^3\Sigma^-)$ (0,0) band at 336 nm can be observed [19, 33], interfering with the N_2 emission, but sometimes enabling more reliable wavelength calibration. In our case, however, the $NH(A-X)$ emission was not observed. With the 3600 g/mm grating, also finer features in the band head were observable, which helped to match the wavelengths of the simulation and measurement correctly. Nevertheless, an iterative approach, of adjusting the wavelength calibration and the rotational temperature until the best possible fit is obtained, is strongly advised. Wrong wavelength calibration results in serious error of the rotational temperature. Although

[§] Please note that all shown simulations have y-data proportional to photon flux, *not* intensity.

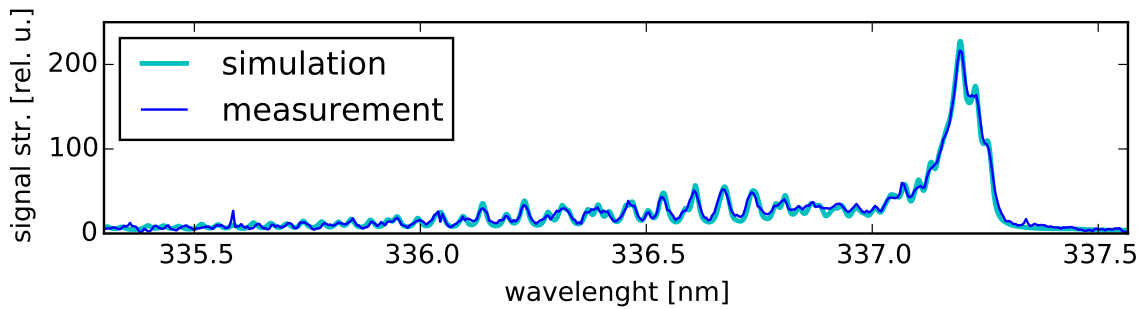


Figure 3. An example of the $N_2(C-B)$ (0,0) band emitted by positive streamer discharges at water interface. The shown spectrum was measured at the point of the triple-line (bottom part of the discharge). The shown simulation is for rotational temperature of 371.7 K.

non-equilibrium population distribution of rotational levels of the $N_2(C)$ state were reported e.g. in chapter 4.2.4 of [1], it was not observed in our conditions. Indeed, the theoretical spectrum, assuming Boltzmann distribution, fits the experimental data very well, see figure 3. After the three coefficients^{||} for wavelength calibration were found, the constant offset term was optimised for each row of the measurement. In this step, the partially binned measurements shown in figure 2 for wavelength calibration were used for the variable wavelength calibration. The signal strength was insufficient for eventual corrections of the first and second order coefficients, these were thus considered constant. Closer inspection of all fits did not reveal any serious violation of this assumption.

When all wavelength calibration coefficients were known, the spatial integration was performed. To avoid unnecessary losses of spectral resolution, a spectra-matching function from *massiveOES*[¶] package was used [18, 19]. For reliable spectral fitting, sufficient signal-to-noise ratio is necessary. This can be enhanced by spatially integrating over wider range. Spatial integration, on the other hand, reduces spatial resolution. To achieve the optimal trade-off, a threshold for signal strength (fivefold of the maximal strength in the ensemble of partially binned data) was selected. The limits for the spatial integration were then selected such that each spatial range after integration gave sufficient signal. In this way, the spatial resolution is variable but never reduced more than necessary.

This approach resulted in two `massiveOES.MeasuredSpectra()` instances, containing spatially resolved spectra of $N_2(C-B)$ for positive and negative streamer discharges (see section 4.1 for explanation of the labels). These were then processed in the *massiveOES* programme assuming Boltzmann distribution to obtain the rotational temperatures as in [19].

The pre-processing of the OH spectra was analogous. The wavelength-matching

^{||} The wavelength of a measured point is calculated from pixel position by second order polynomial.

[¶] The source code is available at the reference URL. The mentioned function is `match_spectra()` from the file `spectrum.py`.

had to be performed for each spectral window separately. The identification of OH(A-X) spectra is more satisfying than that of N₂(C-B). The whole matter was, however, complicated by the fact, that in our case, the spectrum did not follow a single-temperature Boltzmann distribution. For the sake of matching the measurement with the simulation, it is advisable⁺ to assume lower temperature (hundreds K) for wavelengths in the range (308–310) nm but higher temperature (thousands K) for wavelengths above 310 nm (comp. results – figure 10). The spatial integration was also performed analogously, focusing on comparable signal strength rather than on equal integration domains. After that, the spectral windows were attached to a single window. These results were then compared with the simulation. Nevertheless, the fits assuming a single-temperature Boltzmann distribution were unsatisfactory, see example in figure 9(a). A novel method for spectral evaluation was thus developed and is described below.

When the assumption of Boltzmann distribution fails, another approach needs to be taken. The whole procedure of preparing a synthetic spectrum^{*} is preserved, except for assuming anything about the relative populations. Instead, a single synthetic spectrum is calculated for *each rovibronic state* in question, i.e., state that emits lines in the observed wavelength region. Relative population of each state is then treated as a fit parameter. The resulting best-fitting spectrum is a linear combination of these fractional spectra. The problem[‡] can be mathematically formulated as

$$\min_{n_{(J',N',v')}} \left\| m(\lambda) - \sum_{(J',N',v')} n_{(J',N',v')} s_{(J',N',v')}(\lambda) \right\|^2 \quad (1)$$

with the restriction that $n_{(J',N',v')} \geq 0$. In this formula, $m(\lambda)$ is the measured spectrum as a function of wavelength λ and $s_{(J',N',v')}(\lambda)$ are the respective fractional simulated spectra for each upper state, defined in the same points as $m(\lambda)$. (J', N', v') are the three quantum numbers that define a rovibronic state, for details see [36, 37]. The optimised parameters $n_{(J',N',v')}$ are the relative populations of the respective rovibronic states. Example of a state-by-state fit is shown in figure 9(b). Dividing each with its degeneracy $(2J' + 1)$ and plotting its logarithm versus the energy of the levels, a traditional Boltzmann plot can be constructed and analysed.

The state-by-state fitting functionality was incorporated into the *massiveOES* package [18, 19], together with a convenient tool to visualise contributions of selected states to the spectrum. This facilitates the inspection of the fit and the reliability can be judged easily.

⁺ This applies to discharges in contact with liquid water [34, 35] and with excessive abundance of water vapour. There are also discharges with equilibrated distribution of OH(A) rotational levels [19].

^{*} Using a database with wavelength–emission coefficient pairs, calculating line broadening and spectral matching to the measurement, see [19].

[‡] Implementation can be found in the file `MeasuredSpectra.py`, method `fit_nnlis()` of the class

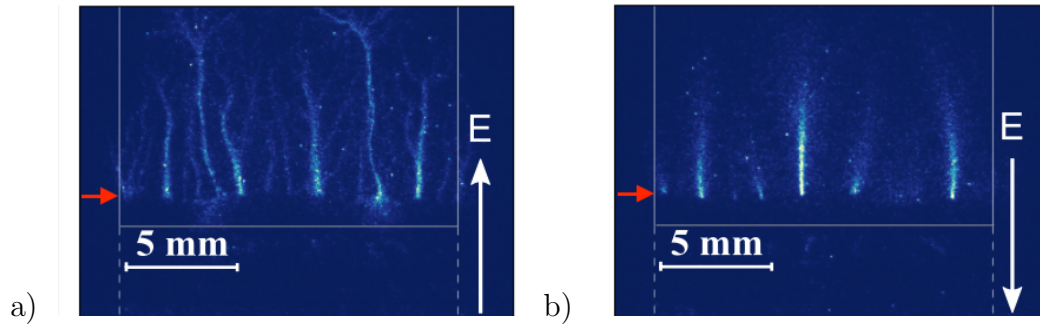


Figure 4. Intensified CCD camera photographs of positive a) and negative streamer discharges b). The vertical grey lines denote the edges of cuvette and the horizontal the water surface. The red arrow denotes the elevated water interface wetting the fused silica surface of the cuvette, i.e. the triple-line. While for positive streamers the length and tree-like structure is similar for all filaments, for the negative streamer discharges the size and the intensity differ from case to case. At some cases just a cathode spot is visible, without a pronounced diffuse jet.

4. Results and discussion

In following chapters, we firstly describe the overall behaviour and features of the generated plasma. Using the intensified CCD imaging we reveal the spatial structure of the typical filaments for both polarities and generally describe their mechanisms. As a next step the undertaken electrical measurements clarify the temporal scale of the discharge current pulses and estimate the power balance during the applied voltage period. Finally, the spectroscopic analysis will be conducted on recorded spatially and phase-resolved spectra of already introduced discharge and the results of novel state-by-state temperature-independent fitting procedure will be discussed.

4.1. Intensified CCD imaging and electrical characterization

After switching-on the applied voltage, the discharge starts in irregular manner and it takes approximately ten minutes until the spatiotemporally stable argon/water interface is established on the surface of the fused silica dielectrics. In such stable mode the discharge takes a filamentary form of usually several filaments propagating from the approx. 1.5 cm long triple-line upwards, along the dielectric surface. This situation is depicted in Fig. 4 where intensified CCD images of the discharge are taken for positive and negative polarity of applied voltage. The discharges stochastically appear at different positions, so at longer exposures, the plasma appears spatially rather homogeneous.

Typically, the surface barrier discharge polarity is designed by the voltage applied on to the upper (not embedded) electrode [38, 39]. We follow this notation although the voltage is applied to the embedded in oil isolated electrode (for safety reasons). As

MeasuredSpectra.

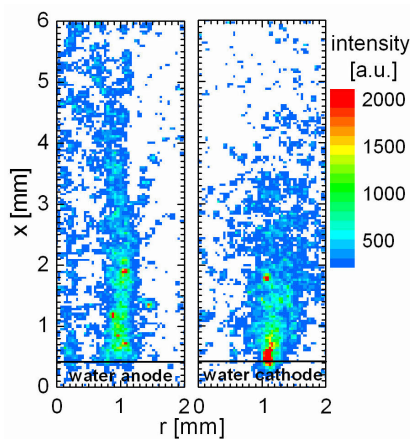


Figure 5. Close-up ICCD images of the typical PSD (left) and NSD (right) discharge filaments emerging from the triple-line of deionised water interface and propagating along the fused silica dielectrics.

a result we describe the discharges propagating during the positive applied half-period as negative streamer discharges (NSD, propagating along the anodic dielectric from cathodic water interface) and positive streamer discharges (PSD) during the negative half-period of the applied voltage.

The structure of the PSD shown in Fig. 4a) is typical for surface positive streamers, resembling a pronounced tree-like structure with relatively homogeneous light emission intensity along its span. Taking into account the length of the filaments, the intensity of light emission and the time scale of the generated current pulses (see further in the text), we can say that the discharge mechanism of PSD is of streamer nature and no significant transition to the leader discharge (as reported e.g. in [40]) takes places in our case.

For NSD, the diffuse structure resembles a cometary shape with most intense light emission at the connection with the negative triple-line interface. These intensive spots at the negative electrode are sometimes called tufts [41] or hot-spots of the strong sheath region (due to the elevated gas temperature at their location, see in [22]). We prefer the term cathode spots [40, 42, 43] as the high-electric-field region was identified as cathode layer created after the micro-sized positive streamer-like ionizing wave arrives to the cathode [42, 44]. We assume that the same mechanism takes place also here at the negative triple-line water interface of the surface barrier discharge (compare [44]).

Analysing the single filament emission intensity in more details we can distinguish the above mentioned features in Fig. 5. We picked up typical filaments for both polarities and plotted their emission intensity along their axial and radial dimensions. The elevated intensity of the cathode spots for the NSD at the triple-line is clearly visible. PSD resembles a tree with homogeneously intensive stem emission and branching while NSD is created by cathode spot and diffusive cloud above.

The results of electrical measurements can be seen in Fig. 6 showing the development

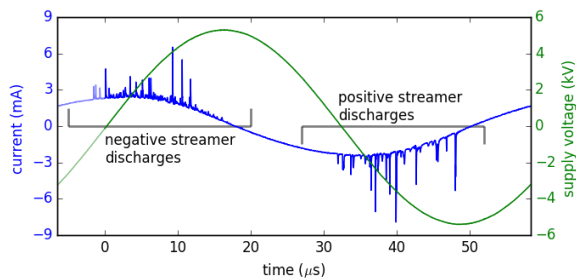


Figure 6. Electrical measurement of current and voltage with denoted 'positive streamer discharges' and 'negative streamer discharges' intervals.

of applied voltage and external circuit current waveforms. Also, intervals of temporal integration of intensified CCD during which the imaging and spectral data were accumulated are denoted there. Note that first discharges for given voltage half-period starts during the end of the preceding one. This is so-called backward-discharging effect caused by the effectively high electric field in the gap advantageously biased by the residual surface charges from discharges of previous polarity [38].

Close-ups of current pulses for each half period are shown in figure 7. Negative streamer discharges show pulses with mean full width half maximum (FWHM) of 15 ns and with wide variety of amplitudes, from units down to tenths of milliamperes. Presumably, the creation process of some of the cathode spots is not finished and they are not able to feed the filament with sufficient current for given local conditions at the interface (locally stored surface charge, solvated electrons in water or generally change in conductivity of plasma-treated deionised water [45]). Thus, their progress does not continue regularly to negative streamer which causes pulses of different amplitudes. During the negative applied voltage half cycle, a lower number of PSD breakdowns occurs and they feature lower variation of amplitude and mean pulse FWHM of 30 ns. In both polarities the maximum peak values of the current pulses are few milliamperes, which is in agreement with measurements performed on barrier discharge filaments in atmospheric pressure argon [46].

Power loss in reactor chamber calculated from electrical measurements data is 1.45 W. Rough estimate of power consumed in discharges is 0.8 W while the rest goes to capacitive losses.

4.2. Rotational temperature of $N_2(C)$

The rotational temperatures of $N_2(C)$ obtained from the fits are shown in figure 8. The spatial integration limits are represented by the spans of the horizontal lines. The vertical span of the coloured region illustrates an estimate of the 68% confidence interval (one standard deviation). This uncertainty is estimated from the fitting procedure itself, assuming that the wavelength calibration and the instrumental broadening are precisely known. It is therefore likely that the shown uncertainty is underestimated.

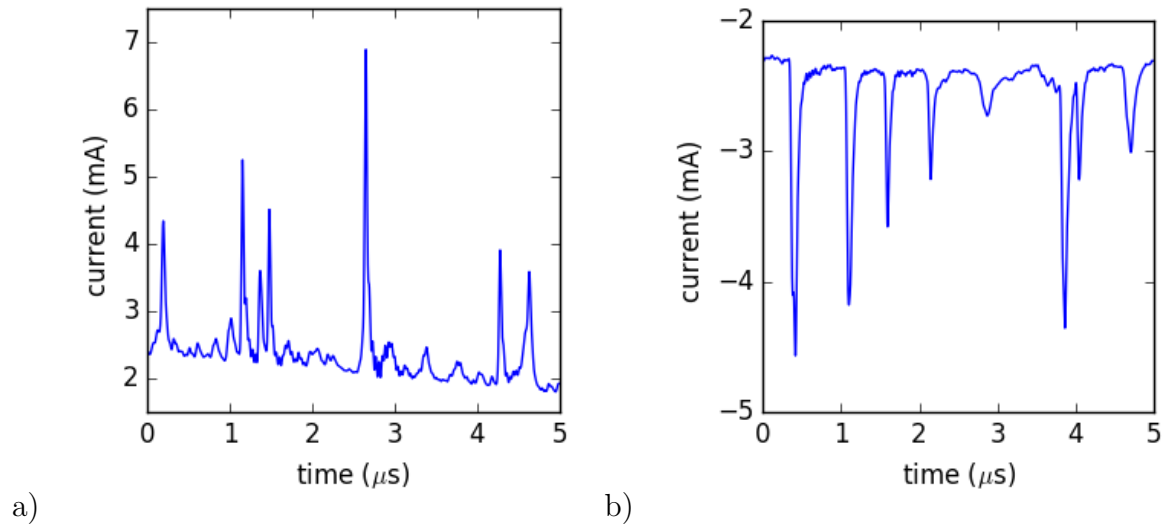


Figure 7. More detailed views on current measurements for ‘negative streamer discharges’ (a) and ‘positive streamer discharges’ (b) intervals. Note large number of smallish current pulses in the ‘negative streamer discharges’ phase.

In figure 8 it can be seen that the gas temperature is about 100 degrees higher than the room temperature (ca. 294 K). The power dissipated in the discharges is rather low (see section 4.1), yet sufficient to significantly increase the temperature in the discharge channels. Our measured temperatures are, as expected, lower than in the case of similar high-power industrially-used setup investigated in [47].

The rotational temperature at the water level (0–0.4 mm) is remarkably similar for positive and negative streamer discharges. In the case of positive streamers, the temperature rises with the distance until the last observable point around 5 mm. The rotational temperature near the triple-line of surface barrier discharge is usually higher for positive streamers [43] with the exception of the location of cathode spots in opposite polarity. The tendency of increasing rotational temperature with increasing distance from the triple-line is unexpected for PSD, as it is opposite to the surface barrier discharge case in air [43]. This can be caused by different heating mechanisms of the positive streamer in argon than in air. Possibly, a not fully developed leader initiation could affect the spectra, as the transition to the leader mechanism in atmospheric pressure argon seems to be much faster/easier than for air [40]. In NSD however, the concave tendency of the temperature dependency on spatial coordinate is similar to that one observed in air [43]. The elevated temperature at the triple-line interface is caused by the presence of cathode spots. There, in high-gradient temperature and electric field region, the rotational temperature determined from $\text{N}_2(\text{C})$ can under certain conditions even reach much higher values than in the positive streamer discharge. In order to resolve the exact mechanism of $\text{N}_2(\text{C})$ rotational energy distribution and heat transfer under given conditions, a well spatiotemporally resolved investigation is needed.

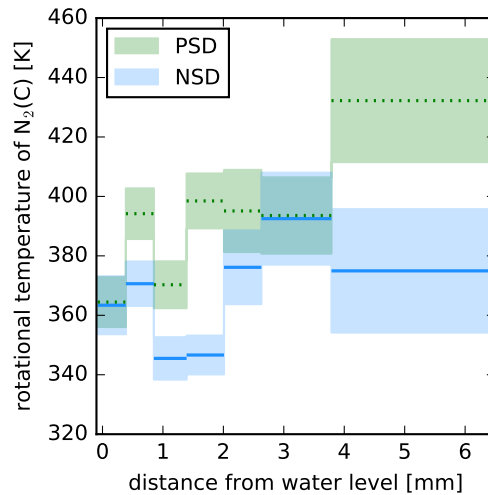


Figure 8. Rotational temperature of $N_2(C)$ along the discharge. PSD (dotted) – positive streamer discharges, NSD (solid) – negative streamer discharges.

4.3. $OH(A-X)$ emission analysis

Boltzmann plots were constructed for each spatial coordinate from state-by-state spectra fitting. In Fig. 9, an example of the fit is shown together with temperature-bound fit for comparison. A typical example of Boltzmann plot is shown in figure 10. This result at first sight resembles similar results obtained in works of others [1, 34, 35]. It should be noted, that in this case the Boltzmann plot was obtained using not a single rotational line, but using all lines from the respective upper state at once, even the overlapping ones. The general characteristics of the Boltzmann plot is the same as in the references. We observe a *cold group* and a *hot group* with greatly different temperatures. We adapt the explanation of Ochkin [1], that the cold group consists of radicals that were in thermal equilibrium with the neutral gas and only recently were excited by an electron impact or a collision with a metastable particle (argon or nitrogen). The rotational distribution of this group should be in good agreement with the translational temperature of the neutral gas. The hot group consists mostly of radicals in the excited electronic state (A) that appeared as an immediate result of water dissociation. During this process, the water molecule bent at ca. 104° gets excited to the B^1A_1 state, where the angle straightens to 180° . This is followed by dissociation to rapidly rotating $OH(A)$ radical and a hydrogen atom.

In the literature, it seems that the traditional way is fitting a single exponential to states with $N' < N'_{\max}$ [17, 34, 35], where N_{\max} is typically around 10 (few units above or below, depending on the discharge conditions). Such approach to our data gives results in the range (350–480) K, mostly depending on the arbitrarily chosen value of N_{\max} , see figure 11. The temperature range satisfactorily overlaps with the results from $N_2(C)$ spectra, compare with figure 8. However, such approach is inconsistent with Ochkin's

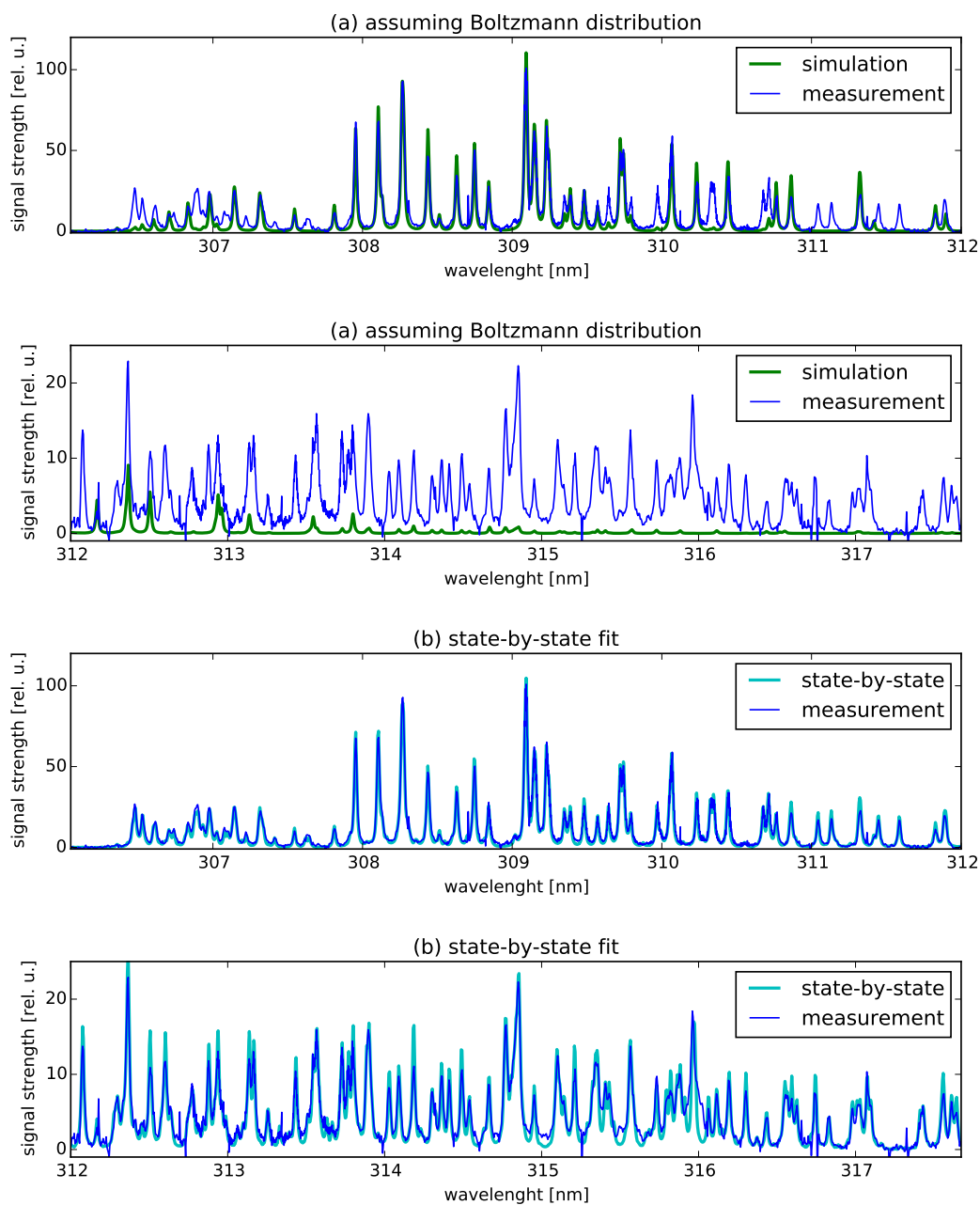


Figure 9. Example of the fits (a) assuming Boltzmann distribution, best fitting $T_{\text{rot}} = 848 \text{ K}$ and $T_{\text{vib}} = 5300 \text{ K}$, (b) state-by-state fit not assuming any population distribution. The Boltzmann plot corresponding to (b) is in figure 10.

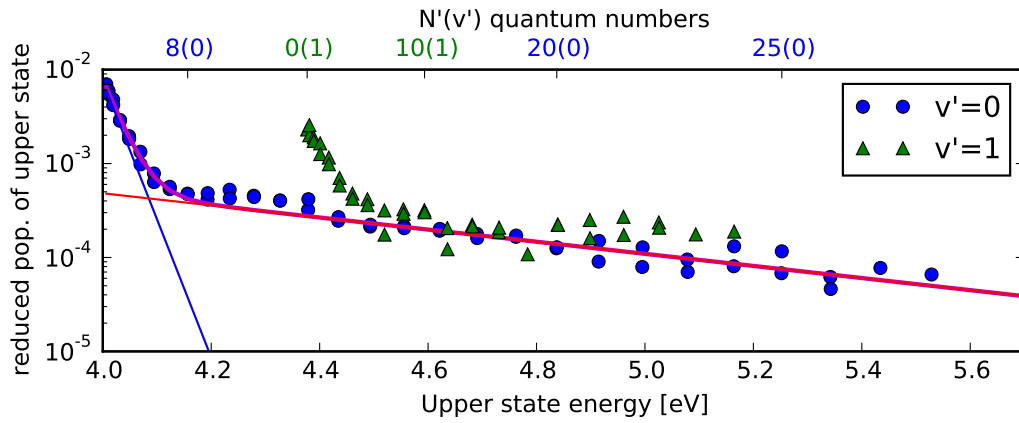


Figure 10. Boltzmann plot from spectrum in figure 9(b). The relative populations are divided by the respective degeneracy, i.e. *reduced*. The magenta curved line is a two-temperature fit, where the blue and red straight lines are its components. The two fitted rotational temperatures are $T_{\text{rot}}^{\text{low}} = 343 \pm 28$ K and $T_{\text{rot}}^{\text{high}} = 7800 \pm 550$ K. Fitted populations of $v' = 2$ states are not shown.

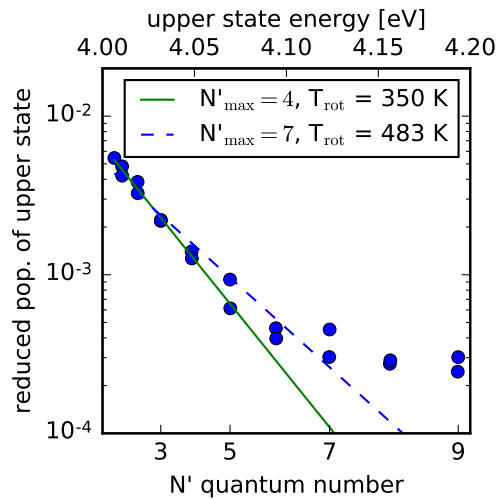


Figure 11. Finding neutral gas temperature from OH Boltzmann plots by fitting a single-temperature Boltzmann distribution strongly depends on the arbitrarily chosen N'_{max} .

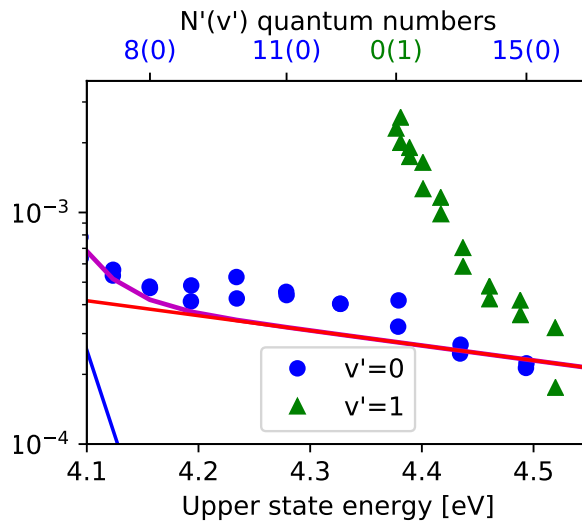


Figure 12. Detail of the Boltzmann plot from figure 10. The population of the states with $9 \leq N' \leq 13$ deviates from the two-temperature distribution and they were excluded from the fit.

explanation of the rotational distribution. The observed population distribution should be a sum of (at least) two independent ensembles of OH radicals in the A state. To reliably obtain the rotational temperature of both, we have thus fitted the observed population distribution with a sum of two independent Boltzmann distributions. This is in principal similar to the treatment proposed by Bernatskiy [48]. A few implementation details, however, should be noted here.

The traditional way of first taking a logarithm of the reduced populations and then fitting a straight line could not be used here. Indeed, a sum of two exponentials cannot be linearised by taking a logarithm. Fitting a sum of exponentials to the distribution of the reduced populations, however, tends to fail, as the populations of states with higher rotational quantum numbers are orders of magnitude smaller and their contribution to the total sum of squares is rather negligible. Even though taking a logarithm does not linearise the problem, it can be used the same way as it is used in plots – to reduce the range of data and enhance the weight of small numbers. For this reason, the minimised expression was

$$\min_{(a_1, a_2, T_1, T_2)} \sum_{(J', N')} \left[\ln \left(a_1 e^{-E_{(J', N')}/(k T_1)} + a_2 e^{-E_{(J', N')}/(k T_2)} \right) - \ln \left(\frac{n_{(J', N')}}{2 J' + 1} \right) \right]^2, \quad (2)$$

a_1 and a_2 are the linear factors for the cold and hot group, respectively, T_1 and T_2 are their respective rotational temperatures. $E_{(J', N')}$ is the potential energy of each state in question. This was performed for $v' = 0$ only, so this quantum number is not present

in the state labels. It is not difficult to perform an equivalent analysis also for higher vibrational states. For such purpose, however, the raw spectra should be measured with greater emphasis on the weaker lines. In this work, for the case of the surface streamer barrier discharge, the signal-to-noise ratio is sufficient only for the analysis of $v' = 0$.

Closer look at the population distribution around 4.3 eV reveals a third group of states, see figure 12. The states with $v' = 0$ and $9 \leq N' \leq 13$ are clearly overpopulated with respect to expectation from the two-temperature fit. To increase the reliability of the two-exponential fit, these states were excluded from the fitting process. The analysis of OH(A-X) spectrum assuming multi-temperature distributions was performed also by Bruggeman *et al.*, see [17], figure 20, though the selected approach was not able to reveal any deviations from two-Boltzmann distributions. All the lines originating from these states were carefully investigated using the Boltzmann-plot inspector tool of the *massiveOES* software. The match of the fitted distribution and the measurement at all spectral regions is strongly convincing that this is a real observation and not an artefact of the method. Possible causes of such overpopulation of this narrow group of rotational states are yet to be found. The selection rules for photon absorption, however, exclude an intense radiation at ca. 4.3 eV, as photons are not allowed to change the rotational states by more than $J \pm 1$. It is more likely, that the residual energy after collision-induced vibrational energy transfer ($v' = 1 \rightarrow 0$) is partially conserved in the rotational states. In environments closer to thermal equilibrium, the population of ($v' = 1$) states is usually orders of magnitude smaller and such effect would not influence the population of ($v' = 0$) states significantly. In this case, however, the population of the ($v' = 1$) state is comparable to the population of ($v' = 0$) state and such effect could indeed be observable. To our best knowledge, this is for the first time such effect has been observed – thanks to the precise analysis enabled by the developed software. However, further investigations are desirable for detailed clarification.

The fitted temperatures from the Boltzmann plots are shown in figures 13 and 14. The lower rotational temperature (figure 13) should hold information about the temperature of the neutral gas and it is expected to agree with the T_{rot} of $\text{N}_2(\text{C})$ shown in figure 8. Some characteristics are, indeed, shared – the temperature in PSD appears to be slightly higher except for the triple-line interface, the temperature profile is concave for NSD and approximately rising for PSD. The absolute values of temperature from OH spectra are, however, about 100 degrees lower. In some cases, the found temperature is even below the expected ambient temperature. Based on the observations presented in this article, it is not possible to precisely determine the origin of this. The match of the two-temperature fit to the measurement, shown in figure 10 supports the two-temperature hypothesis. The rotational temperature of the *cold group* may differ from the translational temperature of the gas. Although it is not quite expected, it should not be excluded in this highly non-equilibrium environment.

The temperature of the *hot group* is shown in figure 14. The interpretation of this parameter is not quite straightforward. Nevertheless, we can compare it to the results of other groups. Bruggeman *et al.* [34] have observed temperatures around 8000 K, Ochkin

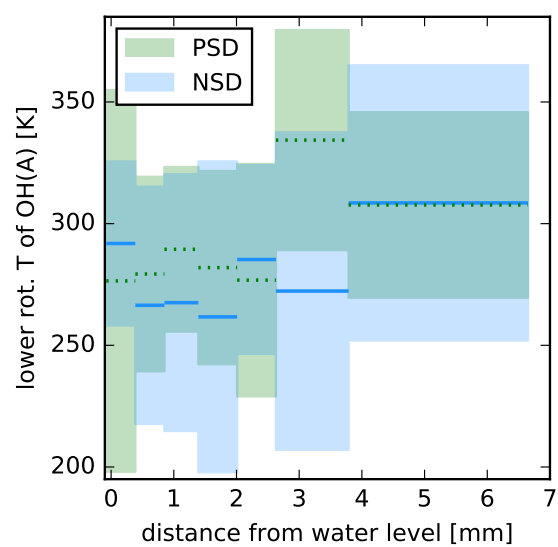


Figure 13. Gas temperature from OH spectra, the lower rotational temperature. PSD (dotted) – positive streamer discharges, NSD (solid) – negative streamer discharges.

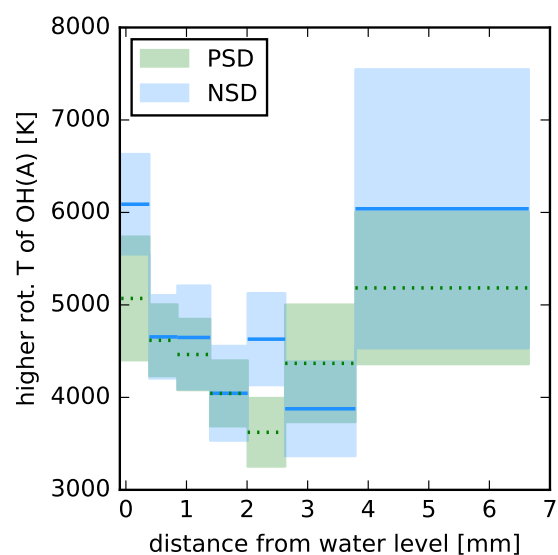


Figure 14. The higher rotational temperature of OH(A). PSD (dotted) – positive streamer discharges, NSD (solid) – negative streamer discharges.

reported temperature of 9000 K [1]. Mohlmann *et al.* have reported temperature as high as 30 000 K – in their experiment, they dissociated water vapour by 100 keV electron beam at low pressure [49]. Voráč *et al.* have observed a single-Boltzmann distribution in a microwave plasma jet [19]. The rotational temperatures of (2 000–5 500) K well matched with vibrational temperature of OH(A).

In this work, we have estimated vibrational temperature from the ratio of populations of $v' = 0$ and $v' = 1$ states, see figure 15. The intensity of lines from $v' = 2$ is insufficient for such analysis. Near the triple-line, the population of $v' = 1$ state even exceeds the population of $v' = 0$ state and the “vibrational temperature” acquires negative values for both polarities (not shown in 15). The spatial profile qualitatively well agrees with the spatial profile of tail (higher) rotational temperature – both are concave and in both cases, the temperature of negative streamer discharges seems to be higher. This is in contrary to the gas temperature. This can be interpreted as follows. The electron-heavy particles collisions are more likely to excite the electronic and vibrational states of the molecules. Afterwards, the energy during heavy particle collisions gradually changes to rotational and translational form. At the time of light emission, the relaxation from electronic and vibrational states to rotations and translational motion (often called E-T, E-R, V-T and V-R relaxation) has advanced further in the PSD than in the NSD. The concentrations of collision partners are not expected to change significantly during the discharge period. Therefore, this is to be attributed rather to the duration of the discharges. This is around 15 ns for NSD and around 30 ns for PSD, see section 4.1 and figure 7. In this respect the vibrational temperature and the tail rotational temperature both seem to represent an intermediate step between the direct electronic excitation and the final relaxation. They both can be probably used as a vague lower limit for electron temperature.

Another interesting parameter is the portion of OH(A) molecules in the hot group η_{hot} (figure 16) calculated as

$$\eta_{\text{hot}} = \frac{n_{\text{hot}}}{n_{\text{hot}} + n_{\text{cold}}}, \quad (3)$$

where n_{hot} and n_{cold} are the sums of the reduced populations over all rotational states for the hot and cold group, respectively. η_{hot} reflects the OH excitation pathways. At the triple-line, over one third of OH(A) molecules is found in the hot group. These should be a direct product of water dissociation via the B^1A_1 state. This portion monotonously falls with the distance from the water level to approximately one fifth at 5 mm distance. It should be noted, that water can be dissociated also other ways than via the B^1A_1 state [50]. These are then expected to contribute rather to the cold group and perhaps they may also lead to the observed low rotational temperature of the cold group. In this respect, more investigations are desirable.

One of the aims of this work was to compare the estimates of neutral gas temperature from rotational spectra of $N_2(\text{C-B})$ (figure 8) and OH(A-X) (figure 13). There are several approaches to estimate this parameter from the rotational spectra of OH(A-X) transition. The single-Boltzmann spectra fitting (as performed here for $N_2(\text{C-}$

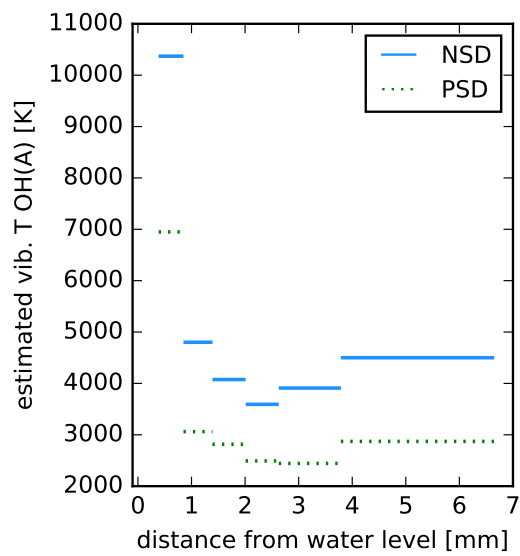


Figure 15. The estimate of vibrational temperature of OH(A). PSD (dotted) – positive streamer discharges, NSD (solid) – negative streamer discharges.

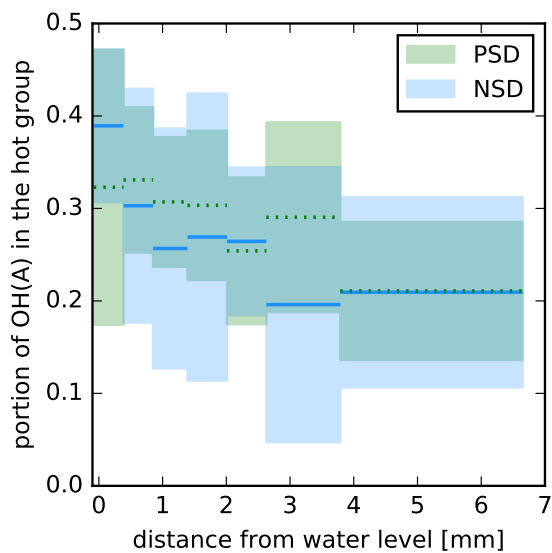


Figure 16. Portion of OH(A) molecules in the hot group. PSD (dotted) – positive streamer discharges, NSD (solid) – negative streamer discharges.

B)) is nowadays already considered unreliable, as was shown previously in [34, 35] as well as in this work (figure 9) – the fitted temperature of 848 K does not reflect any meaningful physical property of the discharge. It is also clear from the mismatch of the single-Boltzmann simulation and the measurement. Preparing a Boltzmann plot and analysing it is thus recommended. Fitting a single-Boltzmann distribution to few arbitrarily selected states with low rotational quantum numbers may be a misleading practice, as the value of result strongly depends on the chosen states. If our understanding of the problem is correct and the rotational distribution is really a sum of two distributions (cold and hot group), the two-Boltzmann fit should be superior. In this case, however, the temperature of the cold group does not agree with the rotational temperature of $N_2(C)$. This may show an unknown process affecting the rotational distribution. In other words, the resulting rotational distribution may be a sum of more than just two distributions.

It should be also noted, that the shown errors in figures 8 and 13 greatly differ in magnitude. The errors in the case of $N_2(C)$ are rather underestimated, see above. Furthermore, the number of degrees of freedom in case of fitting a single-Boltzmann distribution to a whole measured spectrum is much greater than in the case of analysing a Boltzmann plot. This further suppresses the calculated error for $N_2(C)$ temperature. The calculated error in the case of temperatures from the OH Boltzmann plots, on the other hand, seems to be much greater. This, however, reflects the reality as the number of points for the fit is much lower than in the case of the whole spectrum. Also, the four fit parameters (a_1 , a_2 , T_1 , T_2) are rather strongly correlated – i.e. the change of one can be partially compensated by change of other. In this respect, $N_2(C-B)$ spectra seem as a more reliable way of determining the neutral gas temperature. On the other hand, in cases where adding another specie into the discharge is unacceptable, OH spectra may be the only way how to learn something about the neutral gas temperature. In such cases, the proposed way of two-Boltzmann fitting may yield plausible results.

5. Summary and conclusion

A special case of a surface barrier discharge in contact with a solid dielectric and deionised water level was investigated. The driving voltage was sinusoidal. Electrical investigations and ICCD imaging have shown that the discharges appearing in the opposite half-cycles are of fundamentally different nature. The discharges always start at the triple-line interface in contact with the water level. At one half-cycle, positive streamer discharges appear (average duration 30 ns). The negative streamers (average duration 15 ns) emerge in the other half-cycle. Optical emission spectroscopy was performed for the respective half-cycles separately. Spectra of $N_2(C-B)$ and OH(A-X) transitions were recorded and analysed. $N_2(C)$ appeared to be in rotational equilibrium. Assuming, the rotational temperature reflects the temperature of the neutral gas, a temperature profile along the discharge path was constructed for the separate half-cycles. It appeared that the positive streamer discharges are slightly warmer, except

for the triple-line interface, where the temperature was comparable. The temperature in the discharges was in the range (340–440) K.

OH(A-X) spectra revealed a greatly non-equilibrium rotational-vibrational distribution. A novel method of state-by-state fitting has been developed and used to construct Boltzmann plots for each measured spectrum. Preparing a Boltzmann plot may be a difficult task, particularly for overlapping spectra, as noted also in [51]. The proposed state-by-state fitting offers a convenient way to construct Boltzmann plots even from partially overlapping spectra. As this functionality is offered for free as a part of an open-source software package *massiveOES* [18, 19], it is also quite undemanding and available to the community.

The Boltzmann plots were analysed assuming that the observed distribution is a sum of two Boltzmann-distributed independent populations. The states with ($v' = 0, 9 \leq N' \leq 13$) were found to be overpopulated with respect to the two-Boltzmann distribution, perhaps due to fast vibrational-energy transfer. The novel approach to the OH(A-X) spectra enabled us to decouple the different groups of OH(A) and thoroughly investigate their properties. The temperature of the hot group of OH(A) was linked with the vibrational temperature estimate, as they both are believed to show an intermediate step of the E-T and E-R relaxation. This is further supported by the observation, that in the longer lasting positive streamer discharges, both vibrational and hot group rotational temperatures were lower (compared to NSD), while the gas temperature was higher.

The OH(A-X) spectrum was found to be able to provide a rough estimate of the neutral gas temperature. However, due to presence of several indistinguishable excitation pathways that severely influenced the resulting rotational distribution, it is not the preferable way. Whenever possible, thermometry using molecules that are less influenced by chemistry is recommended. Nevertheless, thorough investigations of OH(A-X) spectra with enhanced temporal resolution may bring important insights into the plasma process in transient discharges.

Acknowledgements

This research was funded by the Czech Science Foundation project 16-09721Y. This research has been also supported by the project LO1411 (NPU I) funded by Ministry of Education Youth and Sports of Czech Republic.

The graphs in this publication were composed in the Matplotlib 2D graphics environment [52].

Appendix A. Comment on state-by-state fitting

The simulated fractional spectra $s_{j'}(\lambda, G, L)$ are functions of wavelength λ , and the Gaussian (G) and Lorentzian (L) line broadening parameters. They are thus constant for a particular spectrometer settings (unless a line broadening mechanism comparable to or stronger than the instrumental broadening is present).

The linearity of the problem greatly enhances the computational feasibility and a usual office computer can perform the task in a few seconds. `scipy.optimize.nnls()` function, an implementation of algorithm described in [53], is used for the fit. This approach also allows constructing Boltzmann-plots from spectra with moderate resolution with partially overlapping lines. These are notoriously problematic to obtain from the height of the line [51].

Among the known limitations is particularly the requirement that the number of the considered states must not exceed the number of pixels (the number of the degrees of freedom must be positive). It is also advisable to analyse spectra of molecules with not too few observable lines from one state, as this improves the reliability of the result. A typical example of spectrum not appropriate for this procedure are the bands of $N_2(C-B)$ transition. These bands have strongly suppressed Q-branch and almost completely overlapping P-branch. Effectively, only one line in the R-branch is available for each state, making the fit vulnerable to noise or overlapping lines. Precise wavelength matching of the simulation and the measurement is, of course, essential.

References

- [1] Ochkin V N 2009 *Spectroscopy of low temperature plasma* (Wiley-VCH Verlag, Weinheim) ISBN 978-3-527-40778-1
- [2] Dilecce G 2014 *Plasma Sources Science and Technology* **23** 015011 URL <http://stacks.iop.org/0963-0252/23/i=1/a=015011>
- [3] Šimek M 2014 *Journal of Physics D: Applied Physics* **47** 463001 URL <http://stacks.iop.org/0022-3727/47/i=46/a=463001>
- [4] Laux C O, Spence T G, Kruger C H and Zare R N 2003 *Plasma Sources Science and Technology* **12** 125 URL <http://stacks.iop.org/0963-0252/12/i=2/a=301>
- [5] Bruggeman P and Brandenburg R 2013 *Journal of Physics D: Applied Physics* **46** 464001 URL <http://stacks.iop.org/0022-3727/46/i=46/a=464001>
- [6] Ivković S S, Sretenović G B, Obradović B M, Cvetanović N and Kuraica M M 2014 *Journal of Physics D: Applied Physics* **47** 055204 URL <http://stacks.iop.org/0022-3727/47/i=5/a=055204>
- [7] Navrátil Z, Josepson R, Cvetanović N, Obradović B and Dvořák P 2016 *Plasma Sources Science and Technology* **25** 03LT01 URL <http://stacks.iop.org/0963-0252/25/i=3/a=03LT01>
- [8] Hoder T, Šimek M, Bonaventura Z, Prukner V and Gordillo-Vázquez F J 2016 *Plasma Sources Science and Technology* **25** 045021 URL <http://stacks.iop.org/0963-0252/25/i=4/a=045021>
- [9] Nikiforov A Y, Leys C, Gonzalez M A and Walsh J L 2015 *Plasma Sources Science and Technology* **24** 034001 URL <http://stacks.iop.org/0963-0252/24/i=3/a=034001>
- [10] Zhu X M, Walsh J L, Chen W C and Pu Y K 2012 *Journal of Physics D: Applied Physics* **45** 295201 URL <http://stacks.iop.org/0022-3727/45/i=29/a=295201>
- [11] Janda M, Martišovič V, Hensel K, Dvořák L and Machala Z 2014 *Plasma Sources Science and Technology* **23** 065016 URL <http://stacks.iop.org/0963-0252/23/i=6/a=065016>
- [12] Vašina P, Fekete M, Hnilica J, Klein P, Dosoudilová L, Dvořák P and Navrátil Z 2015 *Plasma Sources Science and Technology* **24** 065022
- [13] Laux C 2002-07 Radiation and nonequilibrium collisional-radiative models, von Karman Institute lecture series
- [14] Luque J and Crosley D 1999 *SRI international report MP 99*
- [15] Western C PGOPHER – a program for simulating rotational structure, Version 9.0.100, University

- of Bristol (2016) URL <http://dx.doi.org/10.5523/bris.1nz94wvrfzddoid67et0t4v4nc>
- [16] Bruggeman P, Verreycken T, González M, Walsh J L, Kong M G, Leys C and Schram D C 2010 *Journal of Physics D: Applied Physics* **43** 124005 URL <http://stacks.iop.org/0022-3727/43/i=12/a=124005>
- [17] Bruggeman P J, Sadeghi N, Schram D C and Linss V 2014 *Plasma Sources Science and Technology* **23** 023001 URL <http://stacks.iop.org/0963-0252/23/i=2/a=023001>
- [18] Voráč J and Synek P 2016 massiveOES software package URL https://bitbucket.org/OES_muni/massiveoes
- [19] Voráč J, Synek P, Potočňáková L, Hnilica J and Kudrle V 2017 *Plasma Sources Science and Technology* **26** 025010 URL <http://stacks.iop.org/0963-0252/26/i=2/a=025010>
- [20] Buehrle J, Herminghaus S and Mugele F 2003 *Phys. Rev. Lett.* **91**(8) 086101 URL <http://link.aps.org/doi/10.1103/PhysRevLett.91.086101>
- [21] Boeuf J P and Pitchford L C 2005 *Journal of Applied Physics* **97** 103307 (Preprint <http://dx.doi.org/10.1063/1.1901841>) URL <http://dx.doi.org/10.1063/1.1901841>
- [22] Stanfield S A and Menart J 2013 *Applied Physics Letters* **103** 054106 (Preprint <http://dx.doi.org/10.1063/1.4817509>) URL <http://dx.doi.org/10.1063/1.4817509>
- [23] Yusupov M, der Paal J V, Neyts E and Bogaerts A 2017 *Biochimica et Biophysica Acta (BBA) - General Subjects* – ISSN 0304-4165 URL [//www.sciencedirect.com/science/article/pii/S0304416517300387](http://www.sciencedirect.com/science/article/pii/S0304416517300387)
- [24] Pavlíňák D, Galmiz O, Zemánek M, Brablec A, Čech J and Černák M 2014 *Applied Physics Letters* **105** 154102 (Preprint <http://dx.doi.org/10.1063/1.4898134>) URL <http://dx.doi.org/10.1063/1.4898134>
- [25] Bruggeman P J, Kushner M J, Locke B R, Gardeniers J G E, Graham W G, Graves D B, Hofman-Caris R C H M, Maric D, Reid J P, Ceriani E, Rivas D F, Foster J E, Garrick S C, Gorbanev Y, Hamaguchi S, Iza F, Jablonowski H, Klimova E, Kolb J, Krcma F, Lukes P, Machala Z, Marinov I, Mariotti D, Thagard S M, Minakata D, Neyts E C, Pawlat J, Petrovic Z L, Pflieger R, Reuter S, Schram D C, Schroter S, Shiraiwa M, Tarabová B, Tsai P A, Verlet J R R, von Woedtke T, Wilson K R, Yasui K and Zvereva G 2016 *Plasma Sources Science and Technology* **25** 053002 URL <http://stacks.iop.org/0963-0252/25/i=5/a=053002>
- [26] Hsieh K, Wang H and Locke B R 2016 *Journal of Hazardous Materials* **317** 188 – 197 ISSN 0304-3894 URL [//www.sciencedirect.com/science/article/pii/S0304389416304915](http://www.sciencedirect.com/science/article/pii/S0304389416304915)
- [27] Thagard S M, Stratton G R, Dai F, Bellona C L, Holsen T M, Bohl D G, Paek E and Dickenson E R V 2017 *Journal of Physics D: Applied Physics* **50** 014003 URL <http://stacks.iop.org/0022-3727/50/i=1/a=014003>
- [28] von Woedtke T, Reuter S, Masur K and Weltmann K D 2013 *Physics Reports* **530** 291 – 320 ISSN 0370-1573 plasmas for Medicine URL [//www.sciencedirect.com/science/article/pii/S0370157313001634](http://www.sciencedirect.com/science/article/pii/S0370157313001634)
- [29] Hsieh K C, Wang H and Locke B R 2016 *Plasma Processes and Polymers* **13** 908–917 ISSN 1612-8869 URL <http://dx.doi.org/10.1002/ppap.201500204>
- [30] Čech J, St'ahel P and Navrátil Z 2009 *The European Physical Journal D* **54** 259–264
- [31] Bruggeman P, Cunge G and Sadeghi N 2012 *Plasma Sources Science and Technology* **21** 035019
- [32] Laux C O and Kruger C H 1992 *Journal of Quantitative Spectroscopy and Radiative Transfer* **48** 9–24
- [33] Janda M, Hoder T, Sarani A, Brandenburg R and Machala Z 2016 Cross-correlation spectroscopy study of the transient spark discharge *23rd Europhysics Conference on Atomic and Molecular Physics of Ionized Gases - proceedings* ed Medvecká V, Papp P, Országh J and Matejčík S (Bratislava: European Physical Society) pp 164–165 ISBN 979-1-09-638902-5
- [34] Bruggeman P, Schram D C, Kong M G and Leys C 2009 *Plasma Processes and Polymers* **6** 751–762
- [35] Nikiforov A Y, Leys C, Li L, Nemcova L and Krcma F 2011 *Plasma Sources Science and Technology* **20** 034008
- [36] Herzberg G and Spinks J W T 1950 *Molecular Spectra and Molecular Structure: Diatomic molecules*

- (Van Nostrand, Princeton) ISBN 978-0894642685
- [37] Voráč J 2014 [cit 2017-01-26] *Plasma diagnostics based on laser induced fluorescence [online]* Dissertation thesis Masaryk universita, Faculty of science, Brno URL [AvailableatWWW<http://is.muni.cz/th/175282/prif_d/>](http://is.muni.cz/th/175282/prif_d/)
- [38] Gibalov V I and Pietsch G J 2000 *Journal of Physics D: Applied Physics* **33** 2618 URL <http://stacks.iop.org/0022-3727/33/i=20/a=315>
- [39] Gibalov V I and Pietsch G J 2012 *Plasma Sources Science and Technology* **21** 024010 URL <http://stacks.iop.org/0963-0252/21/i=2/a=024010>
- [40] Akishev Y, Aponin G, Balakirev A, Grushin M, Petryakov A, Karalnik V and Trushkin N 2013 *Journal of Physics D: Applied Physics* **46** 135204 URL <http://stacks.iop.org/0022-3727/46/i=13/a=135204>
- [41] Stanfield S A and Menart J A 2014 *AIAA Journal* **52** 991–997 ISSN 0001-1452 URL <http://dx.doi.org/10.2514/1.J052402>
- [42] Hoder T, Černák M, Paillol J, Loffhagen D and Brandenburg R 2012 *Phys. Rev. E* **86**(5) 055401 URL <http://link.aps.org/doi/10.1103/PhysRevE.86.055401>
- [43] Stanfield S A 2009 *A Spectroscopic Investigation of a Surface-Discharge-Mode, Dielectric Barrier Discharge* Dissertation thesis Wright State University URL http://corescholar.libraries.wright.edu/etd_all/321/
- [44] Grosch H, Hoder T, Weltmann K D and Brandenburg R 2010 *The European Physical Journal D* **60** 547–553 ISSN 1434-6079 URL <http://dx.doi.org/10.1140/epjd/e2010-00239-8>
- [45] Rumbach P, Bartels D M, Sankaran R M and Go D B 2015 *Nature Communications* **6** 7248 URL <http://dx.doi.org/10.1038/ncomms8248><http://10.0.4.14/ncomms8248><http://www.nature.com/articles/ncomms8248#supplementary-information>
- [46] Kloc P, Wagner H E, Trunec D, Navrátil Z and Fedoseev G 2010 *Journal of Physics D: Applied Physics* **43** 345205 URL <http://stacks.iop.org/0022-3727/43/i=34/a=345205>
- [47] Galmiz O, Pavliňák D, Zemánek M, Brablec A and Černák M 2016 *Journal of Physics D: Applied Physics* **49** 065201 URL <http://stacks.iop.org/0022-3727/49/i=6/a=065201>
- [48] Bernatskiy A, Ochkin V, Afonin O and Antipenkov A 2015 *Plasma Physics Reports* **41** 705–714
- [49] Möhlmann G, Beenakker C and De Heer F 1976 *Chemical Physics* **13** 375–385
- [50] Carr J S and Najita J R 2014 *The Astrophysical Journal* **788** 66
- [51] Van Gessel A, Hrycak B, Jasiński M, Mizeraczyk J, van der Mullen J and Bruggeman P 2012 *Journal of Instrumentation* **7** C02054
- [52] Hunter J D 2007 *Computing in Science and Engineering* **9** 90–95
- [53] Lawson C L and Hanson R J 1995 *Solving least squares problems* (SIAM, Philadelphia)